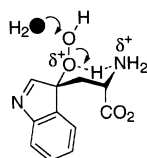


5H7 mIgG (murine), 2.0:1; human polyIgG, 2.1:1. Ratios are based on means of duplicate determinations, except for horse polyIgG, which is the mean of 10 measurements (7).

17. Isotope experiments were also performed with β -galactosidase, the most efficient non-immunoglobulin protein at generating H_2O_2 (see above), as well as 3-methylindole. In both cases, photo-oxidation led to negligible ^{18}O incorporation into the H_2O_2 (Fig. 5, E and F, respectively), illustrating the view that the indole ring itself and tryptophan residues in this protein are behaving simply as reductants of $^1O_2^*$. Irradiation of 3-methylindole generates H_2O_2 that does not include oxygen incorporation from $H_2^{18}O$. The same experiment performed with Trp gives rise to exchange with a $^{16}O/^{18}O$ ratio of 1.2:1. We attribute this result to the ammonium functionality acting as an intramolecular general acid that protonates the internal oxygen of a diastereomeric mixture of 3'-hydroperoxides. This process cannot account for the catalytic production of H_2O_2 by antibodies because it is stoichiometric.

18. D. R. Lide, *Handbook of Chemistry and Physics* (CRC Press, Boca Raton, FL, ed. 73, 1992).



19. M. Detty, S. L. Gibson, *J. Am. Chem. Soc.* **112**, 4086 (1990).

20. C. Deby, *Recherche* **228**, 378 (1991).

21. D. T. Sawyer, *Oxygen Chemistry* (Oxford Univ. Press, Oxford, 1991).

22. J. Cerkovnik, B. Plesnicar, *J. Am. Chem. Soc.* **115**, 12169 (1993).

23. M. A. Vincent, I. A. Hillier, *J. Phys. Chem.* **99**, 3109 (1995).

24. B. Plesnicar, J. Cerkovnik, T. Tekavec, J. Koller, *Chem. Eur. J.* **6**, 809 (2000).

25. E. J. Corey, M. M. Mehrotra, A. U. Khan, *J. Am. Chem. Soc.* **108**, 2472 (1986).

26. J. Koller, B. Plesnicar, *J. Am. Chem. Soc.* **118**, 2470 (1996).

27. F. Cacace, G. de Petris, F. Pepi, A. Troiani, *Science* **285**, 81 (1999).

28. The complex problem of defining theoretically feasible reaction pathways for the conversion of H_2O_3 into H_2O_2 , with or without the participation of $^1O_2^*$, has been tackled in a systematic way using QC methods (B3LYP). This study revealed the existence of a whole spectrum of chemical pathways for the conversion of H_2O_3 to H_2O_2 . Also, extensive docking calculations of H_2O_3 and the transition states for its formation and conversion into H_2O_2 have been investigated for a number of proteins (38).

29. Previous studies suggest that Xe and O_2 colocalize in the same cavities within proteins (30, 37).

30. R. F. Tilson Jr., U. C. Singh, I. D. Kuntz Jr., P. A. Kollman, *J. Mol. Biol.* **199**, 195 (1988).

31. B. P. Schoenborn, H. C. Watson, J. C. Kendrew, *Nature* **207**, 28 (1965).

32. E. E. Scott, Q. H. Gibson, *Biochemistry* **36**, 11909 (1997).

33. T. Prangé et al., *Proteins Struct. Funct. Genet.* **30**, 61 (1998).

34. The structure and sequence around the Xe1 site is almost exactly reproduced in the V_H domain by the pseudo-twofold rotation axis that relates V_L to V_H . Although we did not locate a Xe binding site in this domain, O_2 could still access the corresponding cavity in V_H . The proposed heavy-chain Xe site may not have been found because the crystals were pressurized for only 2 min, due to Xe being too large compared to O_2 for the corresponding cavity on the V_H side, or because of crystal packing. In other antibody experiments, Xe binding sites were found in only one of the two molecules of the

asymmetric unit, which suggests that crystal packing can modulate access of Xe in crystals.

35. Human β_2 -microglobulin, which does not generate H_2O_2 (see above), does not have the same detailed structural characteristics that define the antibody Xe1 binding pocket, despite its overall immunoglobulin fold. Also, β_2 -microglobulin does not contain the conserved Trp residue that occurs there in both antibodies and TCRs. If Trp^{L35} (antibodies) or Trp³⁴ (TCR) is the oxygen sensitizer, the lack of a corresponding Trp in β_2 -microglobulin may relate to the finding that it does not catalyze the oxidation of water.

36. For such a protection mechanism to be effective, catalase must not generate $^1O_2^*$ during H_2O_2 destruction. Currently, there is conflicting evidence regarding $^1O_2^*$ generation from catalase-mediated decomposition of H_2O_2 [see (39)].

37. V. Cannac-Caffrey et al., *Biochimie* **80**, 1003 (1998).

38. D. Datta, X. Xu, N. Vaidehi, W. A. Goddard III, unpublished data.

39. J. R. Kanowsky, *Chem. Biol. Interact.* **70**, 1 (1989).

40. M. Zhou, Z. Diwu, N. Panchuk-Voloshina, R. P. Haugland, *Anal. Biochem.* **253**, 162 (1997).

41. Any concerns that the Amplex Red assay may be detecting protein-hydroperoxide derivatives in addition to H_2O_2 have been discounted, because the apparent H_2O_2 concentration measured using this method is independent of whether irradiated protein is removed from the sample (by size-exclusion filtration).

42. We thank members of the Scripps Research Institute mass spectroscopy facility, especially G. Suizdak and M. Sonderegger, for assistance with the isotope analysis; L. Teyton for the 2C TCR $\alpha\beta$; M. Pique for Kabat database analysis; K. Quon for ICP-AES antibody analyses; B. Zhou for mutagenesis studies; P. G. Schultz for helpful discussions; D. Datta, N. Vaidehi, R. P. Muller, and D. Chakraborty for stimulating discussions; and several Wilson lab members for help with data collection and processing, especially X. Daio. Supported by NIH grants GM43858 (K.D.J.), CA27489 (program project grant; K.D.J., I.A.W., R.A.L.), and HD 36385 (W.A.G.).

16 May 2001; accepted 12 July 2001

The Role of Atomic Ensembles in the Reactivity of Bimetallic Electrocatalysts

F. Maroun,* F. Ozanam,† O. M. Magnussen,‡ R. J. Behm

Bimetallic electrodes are used in a number of electrochemical processes, but the role of particular arrangements of surface metal atoms (ensembles) has not been studied directly. We have evaluated the electrochemical/catalytic properties of defined atomic ensembles in atomically flat PdAu(111) electrodes with variable surface stoichiometry that were prepared by controlled electrodeposition on Au(111). These properties are derived from infrared spectroscopic and voltammetric data obtained for electrode surfaces for which the concentration and distribution of the respective metal atoms are determined in situ by atomic resolution scanning tunneling microscopy with chemical contrast. Palladium monomers are identified as the smallest ensemble ("critical ensemble") for carbon monoxide adsorption and oxidation, whereas hydrogen adsorption requires at least palladium dimers.

Electrocatalytic reactions are of central importance in electrochemistry and play a vital role in emerging technologies related to environmental and energy-related applications, such as fuel cells. The efficiency and selectivity of electrocatalytic processes can be substantially improved by replacing monometallic with bimetallic catalysts. For example, the standard Pt electrocatalysts in polymer electrolyte membrane fuel cells are now being replaced by PtRu and PtMo alloys. The

development of these bimetallic catalysts has been based primarily on empirical grounds. However, a detailed knowledge of the physical origins underlying the improvements in catalytic performance has been lacking so far.

Three explanations have been put forward for the higher activity of bimetallic catalysts: (i) Each metal component could promote different elementary reaction steps, leading to a "bifunctional mechanism" (1). (ii) Electronic effects resulting from interactions between the two metals could improve reactivity (2). (iii) The concept of geometric ensemble effects (specific groupings of surface atoms are required to serve as active sites), developed in heterogeneous gas-phase catalysis (3), has also been suggested for electrocatalysis (4). However, the direct experimental verification or quantitative assessment of the relative contributions of these effects has not been possible up to now. The lack of data on the local atomic arrangement at the surface, both for

Abteilung Oberflächenchemie und Katalyse, Universität Ulm, D-89069 Ulm, Germany.

*Present address: Laboratoire de Physique des Liquides et Electrochimie (CNRS UPR-15), Université P & M Curie, 4 Place Jussieu, F-75005 Paris, France.

†Permanent address: Laboratoire de Physique de la Matière Condensée, CNRS-Ecole Polytechnique, F-91128 Palaiseau, France.

‡To whom correspondence should be addressed. E-mail: olaf.magnussen@chemie.uni-ulm.de (O.M.M.); juergen.behm@chemie.uni-ulm.de (R.J.B.)

real supported electrocatalysts and for model systems, prevented an unambiguous interpretation of electrochemical and spectroscopic data (5).

To clarify these effects, we have developed a simple and robust method for the controlled preparation of surface alloys with well-defined surface composition and flat topography under in situ conditions and identified two different species in a mixed, disordered metal surface by in situ scanning tunneling microscopy (STM) (“chemical resolution”). This allowed us to determine critical ensembles for H adsorption and CO adsorption and oxidation on PdAu(111) electrode surfaces, which show distinct differences in their chemical properties as compared with bulk Pd or Pd monolayer-covered Au(111) electrodes.

In previous electrochemical studies of (surface) alloys, the electrodes were prepared ex situ under ultrahigh-vacuum (UHV) conditions or in a controlled atmosphere and then transferred into the electrochemical environment (6, 7). A much simpler preparation method is to electrodeposit the two (or more) alloy components simultaneously (codeposition). Unfortunately, the deposit in this case sensitively depends on a rather large number

of parameters, such as metal-ion concentrations, deposition potential or current, and mass transport, which makes the reproducible and precise control of alloy composition and morphology difficult. For a more robust preparation procedure, we therefore codeposit the alloy components in a potential regime where the deposition rate is determined solely by the mass transport of the metal ions toward the electrode surface, i.e., where metal-ion reduction at the electrode surface occurs much faster than ion transport in the solution. This deposition procedure allows an accurate control of the composition and the amount of deposited material by simply adjusting metal-ion concentrations and deposition time.

The resulting bimetallic films exhibit a flat morphology with large, flat terraces separated by monoatomic steps, as shown for a monolayer (ML)-thick Pd_{0.7}Au_{0.3} alloy film deposited on a Au(111) single crystal (8) (Fig. 1A). The Au substrate is almost completely covered by such flat deposits. Thicker deposits (up to three MLs) exhibit a similar morphology. This flat morphology of the PdAu deposits on Au(111) is not surprising because the first two MLs of pure Pd (9–11), as well as homoepitaxial Au films (12), both follow a layer-by-

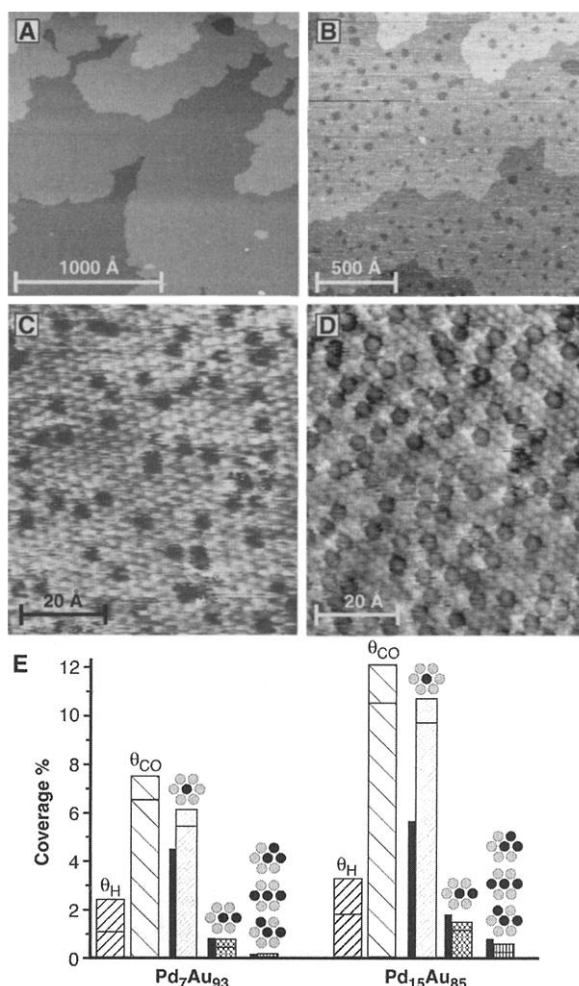
layer growth on Au(111). The Pd content of these films can be determined in a simple way by selective dissolution of the less noble alloy component (Pd) at an adequate electrode potential. Stepping the electrode potential to 0.75 V_{Ag/AgCl} in the presence of Cl[−] in the solution resulted in the formation of monoatomically deep holes in the terraces (Fig. 1B). These holes result from the formation of vacancies caused by Pd dissolution and subsequent vacancy coalescence. The vacancy coverage yields a Pd concentration in the alloy of $\sim 8 \pm 2\%$, very close to the value (7.5%) expected from Pd and Au concentrations and diffusion coefficients in the solution. The uniform distribution of the vacancy islands indicates a homogeneous alloy stoichiometry on the submicrometer scale.

Although STM has been used under UHV conditions to resolve atomic arrangements of alloy surfaces (13–16), atomic-scale data on the local composition of alloy surfaces have not been reported so far in an electrochemical environment. Alloy formation during metal electrodeposition was concluded from morphological changes in the substrate after dissolution of the overlayer (17, 18) or after selective dissolution of one alloy component as in Fig. 1B (6), but not resolved on the atomic scale (19).

The atomic resolution images shown in Fig. 1, C and D, resolve two types of atoms with different apparent heights and shapes. They are arranged in a hexagonal lattice with a lattice spacing equal to that of Au(111). These different features are attributed to Pd and Au atoms, with the majority species corresponding to Au, because the amount of minority species increases with increasing Pd-ion concentration in the solution. From the density of these features, we calculate surface compositions of Pd_{0.7}Au_{0.3} and Pd_{1.5}Au_{0.85}, respectively, in excellent agreement with the expected values.

These STM images allow us to distinguish the surface atomic arrangement in the electrochemical environment. The chemical contrast STM images show that a single, uniform PdAu alloy phase with a disordered metal-atom arrangement is deposited under these conditions. No phase separation in Pd and Au domains occurs, in good agreement with thermodynamic data [mixing enthalpy for Pd in bulk Au, -0.36 eV/atom (20)]. More important, the density of Pd atom ensembles in the surface, such as monomers, dimers, and trimers, can be assessed from a detailed statistical analysis of the images. The coverages of the most frequently observed surface ensembles for Pd_{0.7}Au_{0.3} and Pd_{1.5}Au_{0.85} are plotted in Fig. 1E. The plots show higher concentrations of Pd monomers as compared with random distributions (Fig. 1E, thin bars) (21), equally reflecting the energetic preference for

Fig. 1. (A to D) In situ STM images of PdAu alloys electrodeposited on Au(111). (A) The morphology of a one-ML Pd_{0.7}Au_{0.3} alloy film. (B) The same surface as in (A) after 10-min selective dissolution of Pd at 0.75 V_{Ag/AgCl} in solution containing 10^{−3} M Cl[−]. [(C) and (D)] Atomic resolution images with chemical contrast of (C) Pd_{0.7}Au_{0.3} and (D) Pd_{1.5}Au_{0.85}. Pd atoms appear larger and, depending on tunneling conditions, brighter or darker than Au atoms. (E) Surface coverages of Pd monomers, dimers, and trimers, as obtained from atomically resolved STM images (4000 alloy surface atoms were analyzed for each Pd content), the values expected for a random distribution (thin black bars) (21), as well as corresponding H and CO coverages, derived from the electrochemical data. The error bars correspond to the statistical errors for $\theta_{\text{Pd-Ensemble}}$ to the uncertainties in θ_{H} due to double-layer correction and sulfate coadsorption (29), and to the errors in determining the CO oxidation charge for θ_{CO} , respectively.



Pd-Au bonds. Likewise, the density of dimers and trimers appears to be lower than expected (22).

We combined this microscopic information with macroscopic measurements of electrochemical adsorption and desorption of H and of CO monolayer oxidation on these mixed-electrode surfaces. H adsorbs on Pd electrodes in the range between $-0.2 V_{\text{Ag}/\text{AgCl}}$ and $0.15 V_{\text{Ag}/\text{AgCl}}$, positive to the onset of H_2 evolution, whereas no H adsorption is observed on Au. Current-potential curves of PdAu surface alloys (Fig. 2B) indicate a H adsorption behavior in between that of bare Au(111) and ultrathin Pd films on Au(111) (Fig. 2A). With increasing Pd surface concentration, two pairs of adsorption/desorption peaks gradually emerge—a rather sharp peak around $0 V_{\text{Ag}/\text{AgCl}}$ (α -peak) and a broader one around $-0.1 V_{\text{Ag}/\text{AgCl}}$ (β -peak)—which are similarly observed on Pd(111) (23–25) or Pd deposits on Au(111) (9) and Pt(111) (26, 27), although with different current ratios. The positions of these peaks shift toward positive potentials with increasing Pd concentration, which may result from different adsorption sites or from differences in the electronic structure of the binding surface atoms caused, for example, by increasing Pd coordination [the so-called ligand effect (28)]. The coverage θ_{H} of adsorbed H can be derived by the integration of the current peaks. However, the resulting values should be regarded as an upper limit because of contributions of other electrochemical processes (29). Comparison of θ_{H} with the coverages of Pd ensembles (Fig. 1E) shows that Pd monomers in a PdAu alloy are not able to adsorb H. In addition, H adsorption on Pd dimers and larger ensembles is required in order to account for the measured θ_{H} .

In a similar way, we investigated the oxidation of adsorbed CO, which also adsorbs on bulk Pd, but not on Au(111) electrodes. Current-voltage curves of CO-presaturated PdAu alloy electrodes (Fig. 2C) show a distinct CO oxidation peak around $0.85 V_{\text{Ag}/\text{AgCl}}$, whose charge increases almost linearly with Pd surface content. The peak potential is positively shifted as compared with both Pd monolayer deposits on Au(111) and bulk Pd(111), where it is centered around $0.78 V_{\text{Ag}/\text{AgCl}}$ (Fig. 2A) and $0.64 V_{\text{Ag}/\text{AgCl}}$, respectively (23). This shift already indicates that the Pd surface atoms in the alloy are chemically different from those in a Pd film or bulk Pd.

Further information on CO adsorption and oxidation can be obtained from in situ Fourier transform infrared (FTIR) spectroscopy (Fig. 2D). Spectra of CO-covered alloys with different Pd contents show characteristic peaks at about 2055 and 1910 cm^{-1} , which are typical for linearly and bridge/threefold bound CO adsorbed on metal surfaces. The

peak with opposite sign at 2345 cm^{-1} corresponds to CO_2 in the electrolyte, produced by CO oxidation. The CO high-wavenumber peak first increases in intensity up to 22% Pd surface content, then decreases, and reaches essentially zero intensity for a pure Pd deposit (three-ML Pd film), whereas the low-wavenumber peak emerges at 22% Pd surface content only, and increases substantially at higher Pd content, reaching its maximum intensity for pure Pd films. The CO_2 peak increases linearly with Pd content in the alloy. To account for the CO_2 IR intensities and CO oxidation charges at low Pd contents (7 or 15%), CO must adsorb on the majority of the Pd atoms. Because the density of larger Pd ensembles is too low at these Pd contents, Pd monomers in a Au matrix represent the smallest (“critical”) ensemble size for CO adsorption. The single, high-wavenumber CO IR peak indicates an on-top geometry for CO adsorption on these monomers. The

ratio of the CO IR absorption intensity at 7% Pd content to that at 15% (7:10) suggests that only CO adsorbed on monomers contributes to this peak. On larger ensembles, CO adsorbs in multifold sites, as shown by the data at Pd contents larger than 15%, where the emergence of a substantial surface concentration of larger Pd ensembles coincides with the appearance of the low-wavenumber IR peak, which resembles that observed on Pd(111) at CO saturation coverage (23).

Our studies show that (i) the critical ensemble for CO adsorption on PdAu(111) surface-alloy electrodes is a Pd monomer, (ii) H adsorption from H^+ is not possible on Pd monomers but requires Pd dimers and larger ensembles, and (iii) the chemical properties of small Pd ensembles can differ distinctly from those of ML films or, even more pronounced, of bulk Pd. The approach used in the present work is applica-

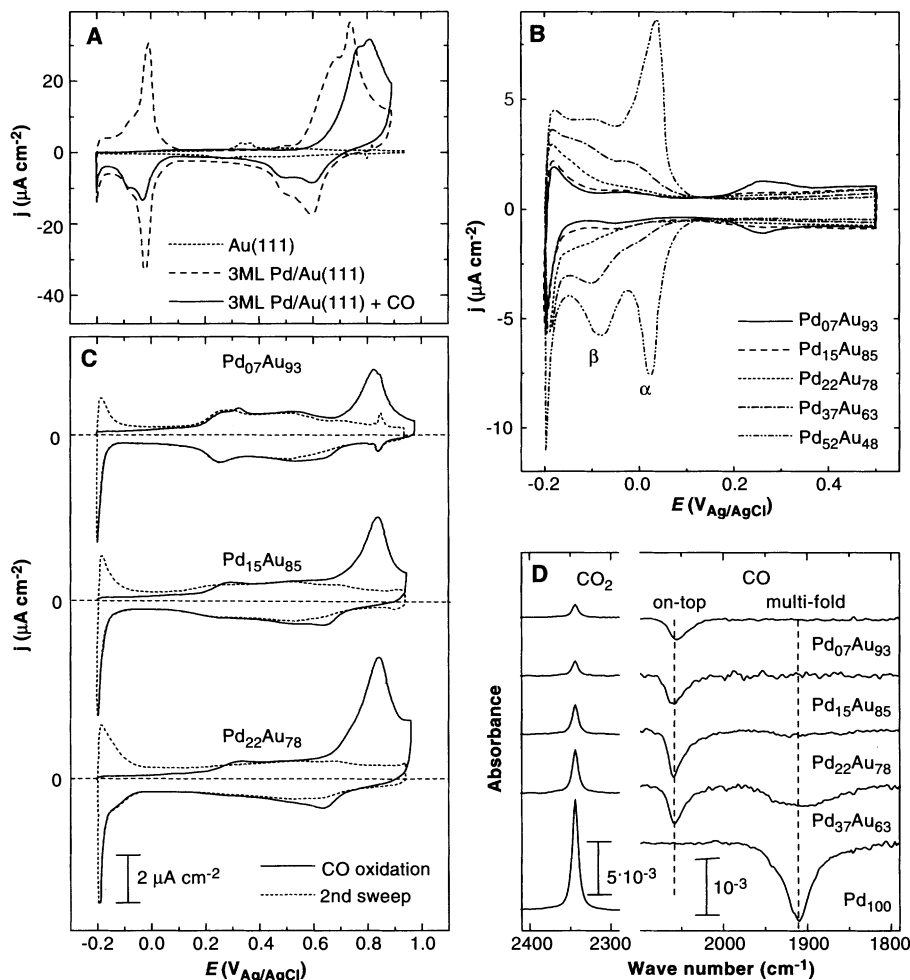


Fig. 2. (A) Dynamic current-voltage curves (10 mV/s) of bare Au(111) and \sim three-ML Pd films on Au(111) in $0.1 \text{ M H}_2\text{SO}_4$ before and directly after CO preadsorption. (B and C) Current-voltage curves of \sim three-ML PdAu alloy films on Au(111), obtained under the same conditions as in (A). Solid and dashed curves in (C) correspond to the first and second cycle after CO adsorption. (D) FTIR absorbance spectra of PdAu alloys. Spectra (~ 2 -min integration time), recorded at $0 V_{\text{Ag}/\text{AgCl}}$ on a CO-presaturated surface, are subtractively normalized to those recorded at $0.9 V_{\text{Ag}/\text{AgCl}}$ after CO oxidation. IR measurements were made in an external reflection geometry with a CaF_2 prism, a $\text{Hg}_x\text{Cd}_{1-x}\text{Te}$ detector, and a FT56000 Bio-Rad spectrometer.

ble for a wide number of bimetallic systems, opening up new perspectives for studying and understanding electrochemical reactions on bimetallic surfaces on a microscopic scale and establishing an atomic-scale mechanism of electrocatalytic reactions.

References and Notes

1. M. Watanabe, S. Motoo, *J. Electroanal. Chem.* **60**, 275 (1975).
2. W. F. Lin et al., *J. Phys. Chem. B* **103**, 6968 (1999).
3. C. T. Campbell, in *Handbook of Heterogeneous Catalysis*, G. Ertl, H. Knözinger, J. Weitkamp, Eds. (Wiley, Weinheim, 1997), vol. 2, p. 814.
4. P. N. Ross, in *Electrocatalysis*, J. Lipkowski, P. N. Ross, Eds. (Wiley, New York, 1998), p. 43.
5. Also for gas-phase catalysis a direct, quantitative evaluation of ensemble/ligand effects had not been possible so far for the same reason, i.e., insufficient information on the exact distribution of surface atoms.
6. R. C. Newman, K. Sieradzki, *Science* **263**, 1708 (1994).
7. H. A. Gasteiger, N. Markovic, P. N. Ross, *Catal. Lett.* **36**, 1 (1996).
8. PdAu alloy films were electrodeposited at 0.3 V_{Ag/AgCl} on Au(111) rotating disk electrodes (2000 rpm) from 0.1 M H₂SO₄ solution (suprapure), containing $x \cdot 10^{-6}$ M K₂PdCl₄ and $y \cdot 10^{-6}$ M KAuCl₄ (pro analysis grade) with $x + y = 3.5$ and the ratio xy equal to 1:9 (Pd₀₇Au₉₃), 1:4 (Pd₁₅Au₈₅), 3:7 (Pd₂₂Au₇₈), 1:1 (Pd₃₇Au₆₃), and 7:3 (Pd₅₂Au₄₈). After rinsing with Milli-Q water the samples were transferred into the cell of the (home-built) STM, into the IR spectrometer cell, or into a separate cell for electrochemical measurements (hanging meniscus geometry, de-aerated with 6.0 Ar), where they were studied in 0.1 M H₂SO₄ solution. CO adsorption was performed at -0.15 V_{Ag/AgCl} by saturating the solution for 10 min with 4.7 CO, followed by 30 min of 6.0 Ar purging.
9. M. Baldauf, D. M. Kolb, *Electrochim. Acta* **38**, 2145 (1993).
10. L. A. Kibler, M. Kleinert, R. Randler, D. M. Kolb, *Surf. Sci.* **443**, 19 (1999).
11. H. Naohara, S. Ye, K. Uosaki, *J. Phys. Chem. B* **102**, 4366 (1998).
12. F. Maroun, F. Ozanam, O. M. Magnussen, R. J. Behm, unpublished data.
13. C. Nagl, O. Haller, E. Platzgummer, M. Schmid, P. Varga, *Surf. Sci.* **321**, 237 (1994).
14. A. K. Schmid, J. C. Hamilton, M. C. Bartelt, R. Q. Hwang, *Phys. Rev. Lett.* **77**, 2977 (1996).
15. B. Sadigh et al., *Phys. Rev. Lett.* **83**, 1379 (1999).
16. B. Gleich, M. Ruff, R. J. Behm, *Surf. Sci.* **386**, 48 (1997).
17. L. A. Kibler, M. Kleinert, D. M. Kolb, *Surf. Sci.* **461**, 155 (2000).
18. M. P. Green, K. J. Hanson, R. Carr, I. Lindau, *J. Electrochem. Soc.* **137**, 3493 (1990).
19. In a single case only, for a ($\sqrt{3} \times \sqrt{3}$) R30° superstructure formed upon TI deposition on Ag(111), in situ STM observations were associated with an alloy formation, but without clear identification of the two metal components (30).
20. F. R. de Boer, R. Boom, W. C. M. Mattens, A. R. Miedema, A. K. Niessen, *Cohesion in Metals: Transition Metal Alloys* (North-Holland, Amsterdam, 1988).
21. M. F. Sykes, M. Glen, *J. Phys. A* **9**, 87 (1976).
22. A similar analysis of alloys with higher Pd content, where larger Pd multimers also contribute substantially, was omitted, because the most important aspects in the chemistry of these surfaces can be understood based on the analysis of low-Pd content data.
23. S. Zou, R. Gómez, M. J. Weaver, *J. Electroanal. Chem.* **474**, 155 (1999).
24. L.-J. Wan et al., *J. Electroanal. Chem.* **484**, 189 (2000).
25. N. Hoshi, K. Kagaya, Y. Hori, *J. Electroanal. Chem.* **485**, 55 (2000).
26. N. M. Markovic, C. Lucas, V. Climent, V. Stamenkovic, P. N. Ross, *Surf. Sci.* **465**, 103 (2000).
27. B. Álvarez, V. Climent, A. Rodes, J. M. Feliu, *J. Electroanal. Chem.* **497**, 125 (2001).
28. Y. L. Lam, J. Criado, M. Boudard, *J. Chim. Phys.* **1**, 461 (1977).

29. Additional contributions to the current come from double-layer charging and sulfate adsorption. The former was corrected by approximating the double-layer capacity of Pd_xAu_{1-x} with a weighted average of those of bare Au(111) and a three-ML Pd film on Au(111), i.e., assuming $C_{PdAu} = x \cdot C_{Pd} + (1-x) \cdot C_{Au}$. The amount of sulfate desorption/adsorption, which occurs on Pd(111) parallel to H adsorption/desorption, cannot easily be assessed for the alloy and considerably contributes to the experimental error in θ_H . Assuming that local sulfate coverage and adsorption charge are similar on Pd ensembles and on Pd(111) [$\theta_{SO_4^{2-},max} = 0.2$ ML, $q_{SO_4^{2-},max} = 90 \mu C cm^{-2}$ (27)], the H coverage will be at most 30% less than that where the contribution of sulfate is neglected.

- an error that does not affect the conclusions on the critical Pd ensemble size.
30. D. Carnal, P. I. Oden, U. Müller, E. Schmidt, H. Siegenthaler, *Electrochim. Acta* **40**, 1223 (1995).
31. We gratefully acknowledge fellowships from "Délégation Générale pour l'Armement" of France and the Alexander von Humboldt foundation as well as financial support by the CNRS and by the Deutsche Forschungsgemeinschaft (BE 1201/6-2). We also thank P. Liu and J. K. Nørskov (Technical University of Denmark) for discussions.

18 April 2001; accepted 31 July 2001

Mantle Flow Beneath a Continental Strike-Slip Fault: Postseismic Deformation After the 1999 Hector Mine Earthquake

Fred F. Pollitz,* Chuck Wicks, Wayne Thatcher

Two recent large earthquakes in the Mojave Desert, California—the magnitude 7.3 1992 Landers and magnitude 7.1 1999 Hector Mine earthquakes—have each been followed by elevated crustal strain rates over periods of months and years. Geodetic data collected after the Hector Mine earthquake exhibit a temporally decaying horizontal velocity field and a quadrant uplift pattern opposite to that expected for localized shear beneath the earthquake rupture. We interpret the origin of this accelerated crustal deformation to be vigorous flow in the upper mantle in response to the stress changes generated by the earthquake. Our results suggest that transient flow in the upper mantle is a fundamental component of the earthquake cycle and that the lower crust is a coherent stress guide coupling the upper crust with the upper mantle.

Mineral physics dictates that beneath the continental upper crust, the temperature of rocks is sufficiently high that the underlying lower crust and mantle flow through various solid state creep mechanisms (1–4). The mechanics of stress evolution in Earth's continental crust remain to be resolved. Central issues are whether strain accumulation in continental shear zones is driven by thick bounding blocks or by localized shear beneath the faults, whether the lower crust flows more or less readily than the upper mantle, and whether faults penetrate to depths substantially greater than seismogenic depths (~15 km in the western United States). Postseismic readjustment of the crust after the 16 October 1999 Hector Mine earthquake (Fig. 1A) carries large signals from potentially deep flow processes, and observations of this readjustment can characterize its mechanism, as well as yield clues to the rheology of the lower crust and upper mantle.

We analyzed synthetic aperture radar (InSAR) and Global Positioning System (GPS)

data collected during the first 9 months after the Hector Mine earthquake (Figs. 1, B, C, and E, and 2, A and B) to determine the postseismic surface velocity field. The Hector Mine earthquake involved about 2 m of right-lateral slip along a 40- to 50-km-long fault (5, 6), and the event altered the rate and pattern of regional aseismic crustal deformation. The InSAR data recorded range change, the change in distance between Earth's surface and an orbiting satellite (7, 8), during the 9-month postseismic epoch. The measured range change is attributed primarily to vertical movement of Earth's surface but is also affected by horizontal movements. A total of three image pairs, covering three different time periods over the first 9 months of the postseismic epoch, were used to construct the interferograms (Fig. 1, B, C, and E) (9). GPS data carry independent information about horizontal and vertical movements, but we restrict our analysis to the horizontal velocity field changes because of their relatively small errors.

Postseismic InSAR deformation exhibits local, near-fault motions, but here we focus on the long-wavelength signal (>~30 km), which exhibits a quadrant pattern. This pattern is similar for the three depicted time periods, as shown by

U.S. Geological Survey, 345 Middlefield Road, MS 977, Menlo Park, CA 94025, USA.

*To whom correspondence should be addressed. E-mail: fpollitz@usgs.gov